Sensors and Materials, Vol. 28, No. 6 (2016) 609–618
MYU Tokyo

S & M 1215

Wireless Inertial Sensors Made on Flexible Substrates and Based on Thermal Convection and Near-Field-Communication Principles

Jium-Ming Lin* and Cheng-Hung Lin[1]

Department of Electronic Engineering, Chung-Hua University,
707, Sec. 2 Wu-Fu Rd., Hsin-Chu, 30012 Taiwan, ROC
[1]Ph.D. Program in Engineering Science, College of Engineering., Chung-Hua University,
707, Sec. 2 Wu-Fu Rd., Hsin-Chu, 30012 Taiwan, ROC

(Received March 3, 2015; accepted February 26, 2016)

Keywords: inertial sensors, flexible substrate, thermal convection, near-field-communication

In this study, several kinds of wireless inertial sensors, such as accelerometers, angular accelerometers and inclinometers based on the thermal convection principle, were integrated with near-field-communication (NFC) antennas and made on a flexible substrate so that the devices can become wireless sensors. The reason to apply a flexible substrate instead of the traditional silicon was to reduce the power leaked through the flexible substrate, because the thermal conductivity of silicon is 0.06–0.0017 W/(cm·K), which is 25 times larger than that of the flexible substrate, 1.48 W/(cm·K). Another key goal was to fabricate the nonfloating-type devices without making a cavity on the substrate, so that the new devices would be easier to fabricate and more reliable than the previous floating-type; in which the components of heaters and thermal sensors lay over the cavity on the silicon substrate. Also inert Xe gas was used to fill the chamber instead of the previously used CO_2 or air, so that the oxidization problem of the thermal sensors caused by the heater can be eliminated. On the other hand, one can fabricate the components of heaters and thermal sensors on the flexible substrate directly or stack them on a layer of aluminum nitride and then use some packages with hemispherical or hemicylindrical chambers instead of rectangular ones. The sensitivities were analyzed and compared with those of the previous sensors to prove the feasibility of these novel ideas.

1. Introduction

Conventional accelerometers, inclinometers, and rate gyros are fabricated on silicon.[1–17] Some are made using thermal convection technologies, and their chambers may be filled with air, CO_2, or liquids. It was reported that the sensitivity of an inclinometer can be increased by using a nonfloating-type structure on a flexible substrate without fabricating the conventional cavities of floating-type silicon-based devices.[7–12] Moreover, the chamber may be filled with an inert gas such as Xe to avoid the oxidizing effect caused by CO_2 or air. Thus, both the reliability and life cycle of heaters and thermal sensors can be increased. In addition, one can apply either a hemispherical or a hemicylindrical chamber to improve the device sensitivity beyond that of the traditional rectangular

*Corresponding author: e-mail: jmlin@chu.edu.tw

ISSN 0914-4935

sensors.[13] On the other hand, the outer shape of the packages can still be rectangular for ease of marking part names and series numbers. Moreover, in this study we fabricated the heater and thermal sensors of accelerometers not directly on the substrate but stacked on a layer of aluminum nitride to enhance the sensitivity. As shown in Fig. 1(a), several kinds of wireless inertial sensors, such accelerometers, angular accelerometers, and inclinometers based on the thermal convection principle, are proposed to further integrate with an active near-field-communication (NFC) tag so we can operate the devices in wireless manner and deploy them anywhere, for example, to monitor the status of bridge safety but also the movements of mudflows and landslides as shown in Figs. 2(a) and 2(b), respectively. This paper is organized as follows: the first section is the introduction; the next part describes the fabrication and packaging steps; the third part is simulation and discussion; and the last part is conclusions.

2. Fabrication and Packaging Steps

The fabrication steps are as follows:

Step 1: Deposit SiO_2 on both sides of a substrate to isolate it from thermal and electrical influences, and from humidity. Then protect the layers of SiO_2 with layer of photoresist (PR) on both sides.

Step 2: Deposit p-type amorphous silicon (green color) at a thickness ranging from 100 to 250 μm, and use a Nd-YAG laser to anneal to form a polysilicon thermister. The thermisters may not be in parallel with each other as shown in Figs. 3(a) and 3(b). Next, cover the front side with a layer of PR (gray color). Using mask #1 and photolithography and etching processes (PAEPs), retain the PR on the thermister to protect the underlying layer of polysilicon. Next, use a KOH solution or an reactive ion etching (RIE) process to remove the unprotected. Figure 3(a) shows the result.

Step 3: Remove the PR. Evaporate Cr and Ni to fabricate the heater, NFC antenna, and the

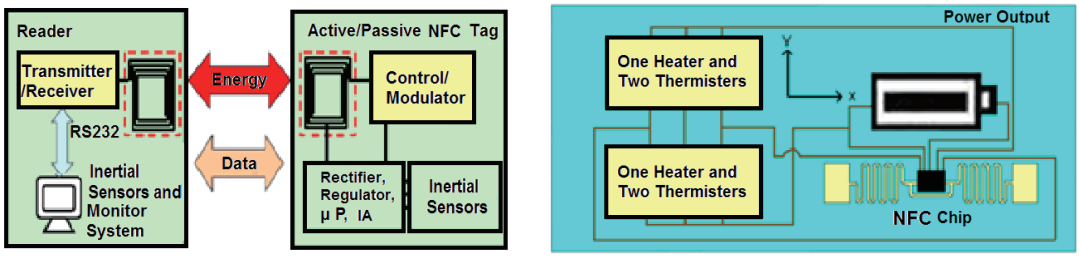

Fig. 1 (Color online) Block diagram of (a) the proposed NFC-based inertial sensors and (b) NFC tag.

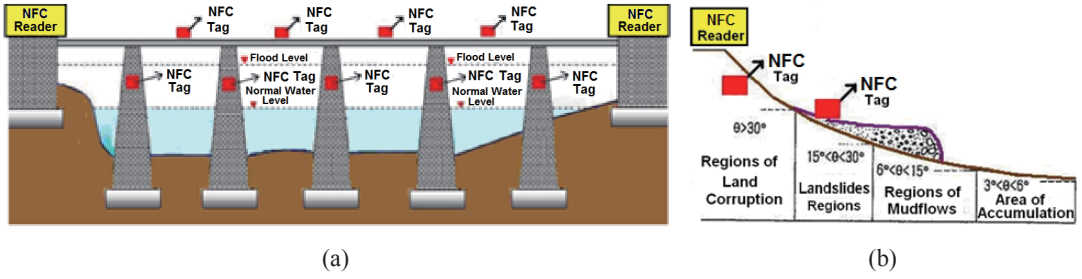

Fig. 2. (Color online) Inertial sensors can be deployed at anywhere to monitor not only (a) the status of bridge safety, but (b) movements of mudflows and landslides.

conductors connected to the power supply. Next, use mask #2 and PAEP to retain the PR on the heater, NFC antenna, and the conductors connected to the power supply. Use a sulfuric acid solution to remove the unprotected layers of Cr and Ni. After the PR is removed, the result is shown in Fig. 3(b).

Step 4: Use mask #3 and PAEP to retain the PR on the heater, and then flash a layer of Au on the Ni layer by electroless plating. The conductivity of the radio frequency identification (RFID) antenna, as well as the conductors connected to the power supply should be very good. In addition, the soldering performance on the pads for packaging should be improved.

Step 5: Print plastic material around the inertial sensors as a dam, and then put a cap with hemispherical, hemicylindrical, or rectangular chamber on the dam for curing. Seal and fill with CO_2 or Xe gas. Finally, the chip is flip-chip-bonded to the antenna feed terminals; then make the underfill to enhance the adherence of the chip. The results are shown in Figs. 4(a) and 4(b).

Step 6: To increase the sensitivity and reduce the drift and bias effects caused by fabrication errors, put four thermisters in a full differential Wheatstone bridge. Use or attach a socket and a spring to fix the battery on the substrate.[18–22] Figure 1(b) shows the top view of the final result.

Note that one can also fabricate the components of heaters and thermal sensors in either a parallel or nonparallel fashion or on a stacked layer of aluminum nitride instead of directly on a flexible substrate. In §§ 3.1 and 3.2, these two options will be discussed regarding the fabrication of an angular accelerometer and an accelerometer, respectively.

3. Simulated Results and Discussion

In this section simulations using the ESI Group's CFD and multi-physics (ESI-CFD+) software package are discussed. One can apply any of the hemispherical, hemicylindrical, and rectangular chambers to either floating or nonfloating structure for comparison. The temperatures of the package boundaries and the heaters were set to 300 and 400 K, respectively.

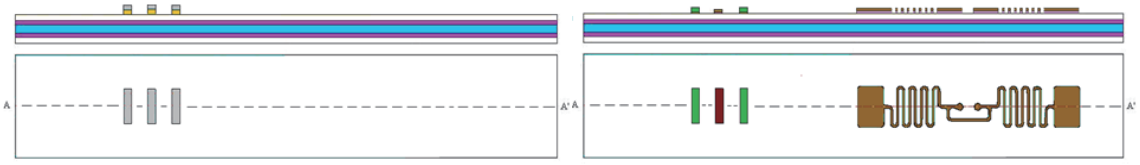

(a) (b)

Fig. 3. (Color online) Results after (a) Step 2 and (b) Step 3.

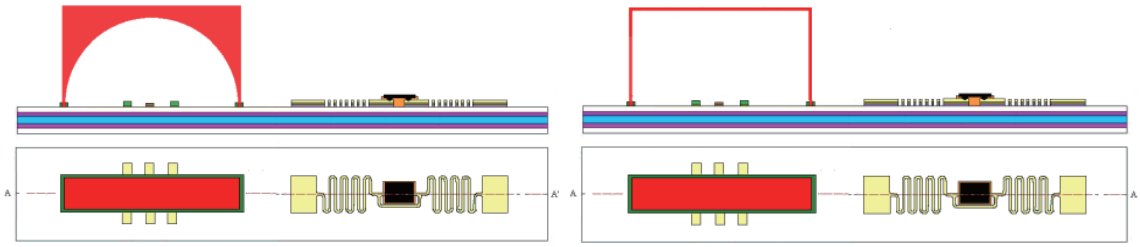

(a) (b)

Fig. 4. (Color online) Results after Step 5 with (a) hemispherical (or hemicylindrical) and (b) rectangular chambers.

3.1 Results for the angular accelerometer

The cross-sections and geometries of hemispherical chambers, heaters, and thermistors in parallel and nonparallel structures are shown in Figs. 5(a) and 5(b). The thermal sensors can be put at any of three points. The distances between the heater and thermal sensors were set at 3 mm. Using the parallel and nonparallel structures, the sensitivities (temperature differences vs angular accelerations) for the thermal sensors at points 1, 2, and 3 are shown in Figs. 6(a) and 6(b), respectively. Note that the device sensitivity using the parallel structure for the thermal sensors at point 2 was better 0.0896 K/(rad/S^2), but there were nonlinear effects. For the nonparallel structure, the sensitivity was reduced to 0.0833 K/(rad/S^2) for the thermal sensors at point 2, but in this case the behavior was more linear. For comparison, the temperature distributions in both vertical and horizontal planes for both types (at point 2) are shown in Figs. 7 and 8, respectively. On the other hand, for a rectangular chamber, as shown in Fig. 9, the sensitivities for the angular accelerometers of floating and nonfloating structures are shown in Figs. 10(a) and 10(b), respectively. Note that the sensitivities are better for thermal sensors located at point 2 using the floating and nonfloating structures. However, the structure and sensitivity of the nonfloating structures are both simpler and also better.

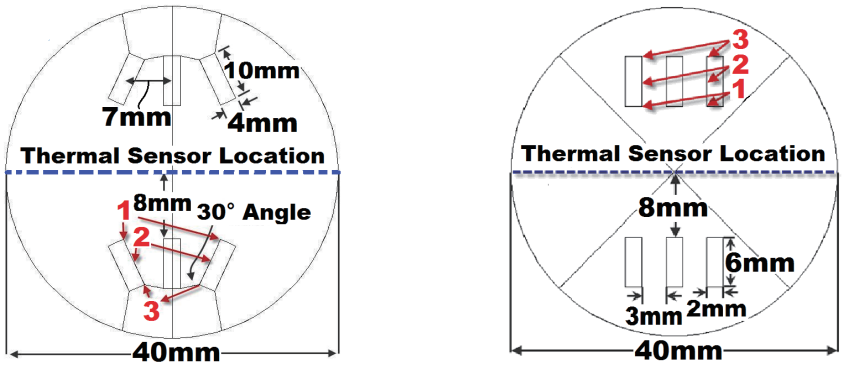

(a) (b)

Fig. 5. (Color online) Cross-sections and geometries of hemispherical chambers, heaters, and thermistors in (a) parallel and (b) nonparallel structures.

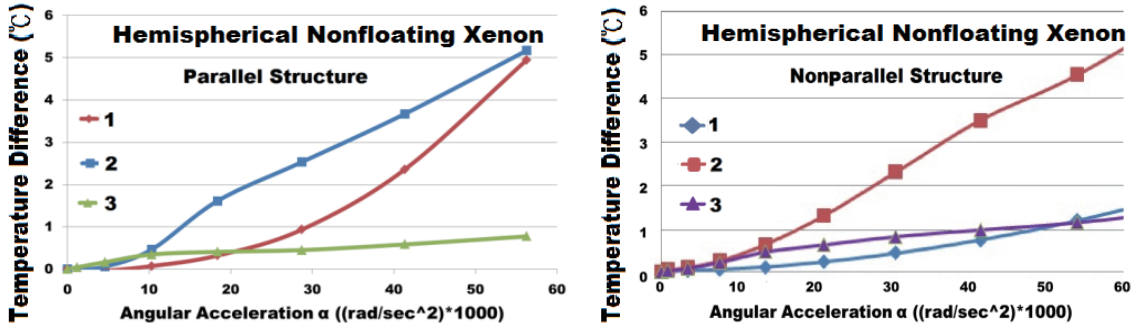

(a) (b)

Fig. 6. (Color online) Sensitivities of angular accelerometers with (a) parallel and (b) nonparallel structures for thermal sensors located at points 1, 2, and 3.

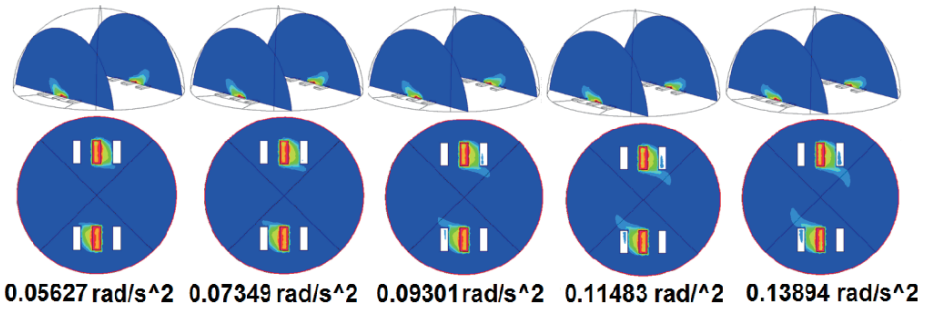

Fig. 7. (Color online) Distributions of temperature in vertical and horizontal planes in the parallel structure.

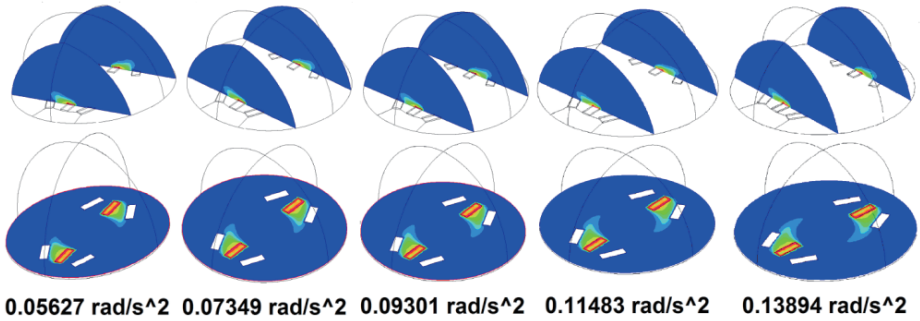

Fig. 8. (Color online) Distributions of temperature in vertical and horizontal planes in the nonparallel structure.

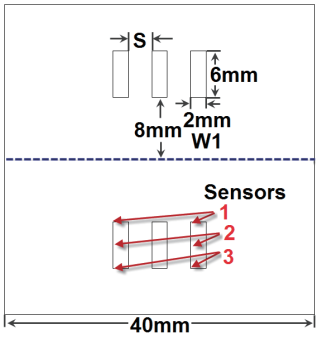

Fig. 9. (Color online) Cross-sections and geometries of heaters, thermistors, and a rectangular chamber.

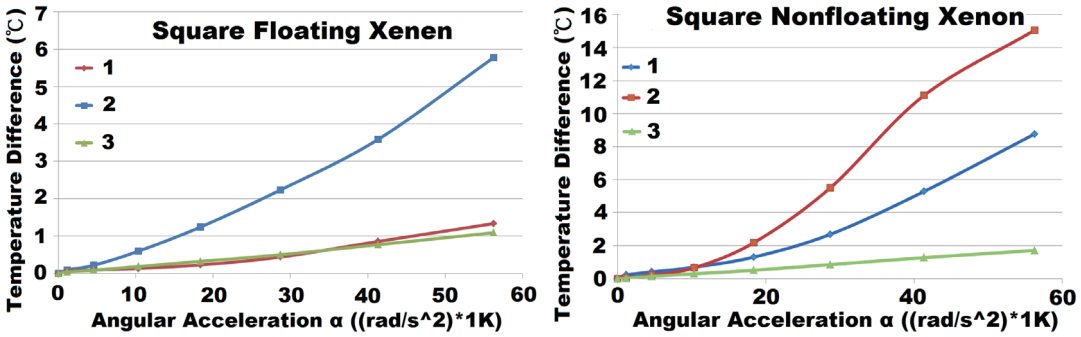

(a) (b)

Fig. 10. (Color online) Sensitivities for a square chamber with angular accelerometers of (a) floating and (b) nonfloating structures for thermal sensors located at points 1, 2, and 3.

3.2 Results for the accelerometer

The cross-sections and geometries of accelerometers with hemicylindrical and rectangular chambers are shown in Figs. 11(a) and 11(b), respectively. The heaters and the thermistors were stacked on layers of aluminum nitride. Other parameters were set as follows: *T1* = 1 mm, *T2* = 0.3 mm, *T3* = 0.3 mm, *S* = 6 mm, *H* = 18.7 mm, and *W1* = 4 mm. The sensitivity curves of the hemicylindrical and rectangular chambers with or without stacked materials and with CO_2 or Xe gas are shown in Figs. 12 and 13, respectively, in which 1 G = 9.8 m/S^2. Note that the sensitivities using a stacked layer and/or Xe gas can be increased. Moreover, Figs. 14(a) and 14(b) show the sensitivity curves for rectangular and hemicylindrical chambers, respectively, with and without stacked layers and filled with CO_2 or Xe gas. The results for the traditional rectangular chamber with either gas without a stacked layer indicate nonlinear effects. However, the linearity is better for accelerations larger than 18 G's, and the case using a hemicylindrical chamber filled with Xe gas with a stacked layer is more linear; the sensitivity is 0.227 °C/G. This moment is listed in Table 1 for comparison.

3.3 Results for the inclinometer

The cross-sectional geometry of the floating inclinometer with a hemispherical or hemicylindrical chamber shown in Fig. 15 was used first. Its dimensions were *W1* = 0.5 mm, *W2* = 0.3 mm, *W3* = 1 mm, *S* = 1.25 mm, and *H* = 8.7 mm. Not shown in Fig. 15 are the length and the floating height (*H1*) of the thermisters and heater, which were 9 and 1 mm, respectively. The

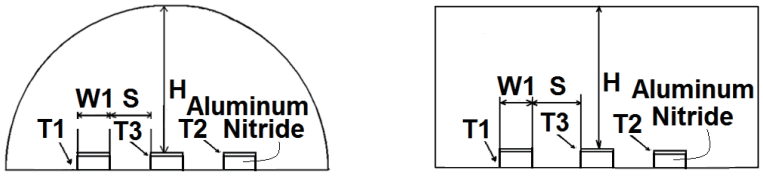

(a) (b)

Fig. 11. Cross-sections and geometries of hemicylindrical and rectangular chambers with stacked layers of aluminum nitride.

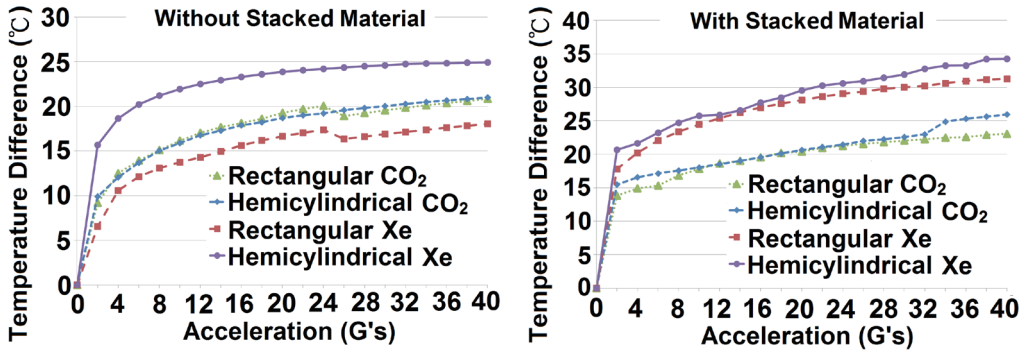

(a) (b)

Fig. 12. (Color online) Sensitivity curves for accelerometers applying hemicylindrical and rectangular chambers and filled with CO_2 or Xe gas, (a) without and (b) with stacked layers.

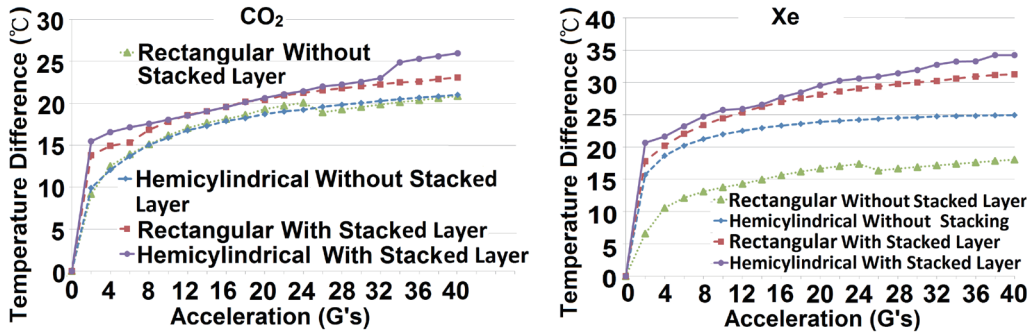

(a) (b)

Fig. 13. (Color online) Sensitivity curves for accelerometers with hemicylindrical and rectangular chambers with and without stacked layers, using (a) CO_2 or (b) Xe gas.

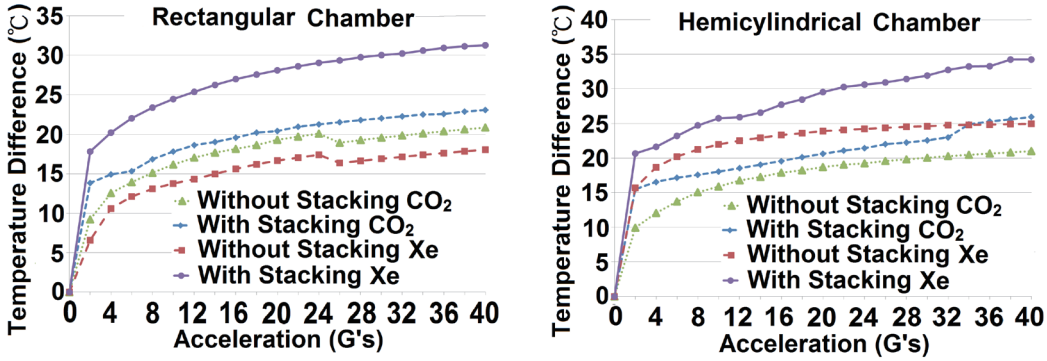

(a) (b)

Fig. 14. (Color online) Sensitivity curves for accelerometers with and without stacked layers and filled with CO_2 or Xe gas, using (a) rectangular and (b) hemicylindrical chambers.

Table 1
Comparisons of sensitivities for various cases.

Chambers	Stacked materials	Xe gas (°C/G)	CO_2 gas (°C/G)
Hemicylindrical	Yes	0.227	Nonlinear
	No	0.045	0.114
Rectangular	Yes	0.182	0.11
	No	Nonlinear	Nonlinear

chamber was filled with Xe or CO_2, and the sensitivity curves (temperature differences at the center points of thermisters vs tilt angles) were determined and are shown in Fig. 16. The sensitivity curves are nonlinear when either Xe or CO_2 was used. Thus the floating structure is not usable, and we tried the nonfloating structure as shown in Fig. 17, in which $W1$ = 0.1 mm, $W2$ = 0.6 mm, S = 1.25 mm, and H = 9.9 mm. The sensitivity results for the nonfloating structure with hemispherical, hemicylindrical, and rectangular chambers are as shown in Figs. 18(a)–18(c), respectively. The sensitivities in the case of filling with Xe gas were always better than those with CO_2, because the molecular weight of Xe gas is three times that of CO_2. On the other hand, one can redraw the sensitivity curves for the chambers filled with Xe or CO_2 as shown in Figs. 19(a) and 19(b), respectively. The performances in the cases with hemispherical and hemicylindrical chambers were

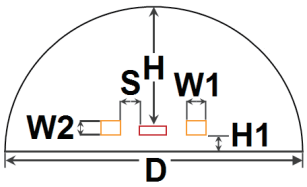

Fig. 15. (Color online) Cross-sectional geometry of the floating inclinometer with a hemispherical or hemicylindrical chamber.

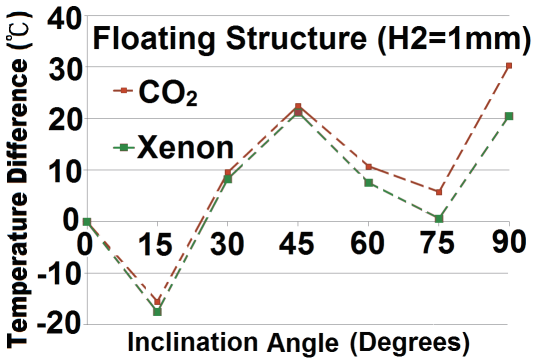

Fig. 16. (Color online) Sensitivity curves of floating inclinometers filled with Xe or CO_2 gas.

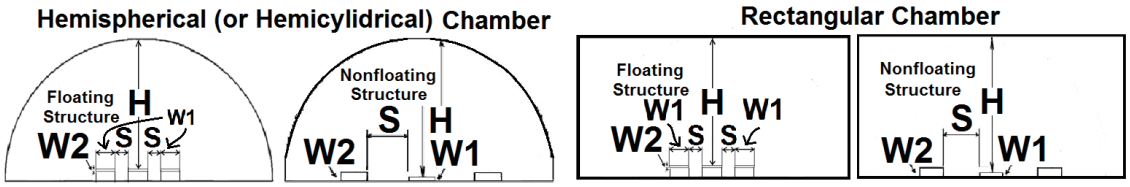

(a) (b)

Fig. 17. Inclinometers using the nonfloating structure with (a) hemispherical (or hemicylindrical) and (b) rectangular chambers.

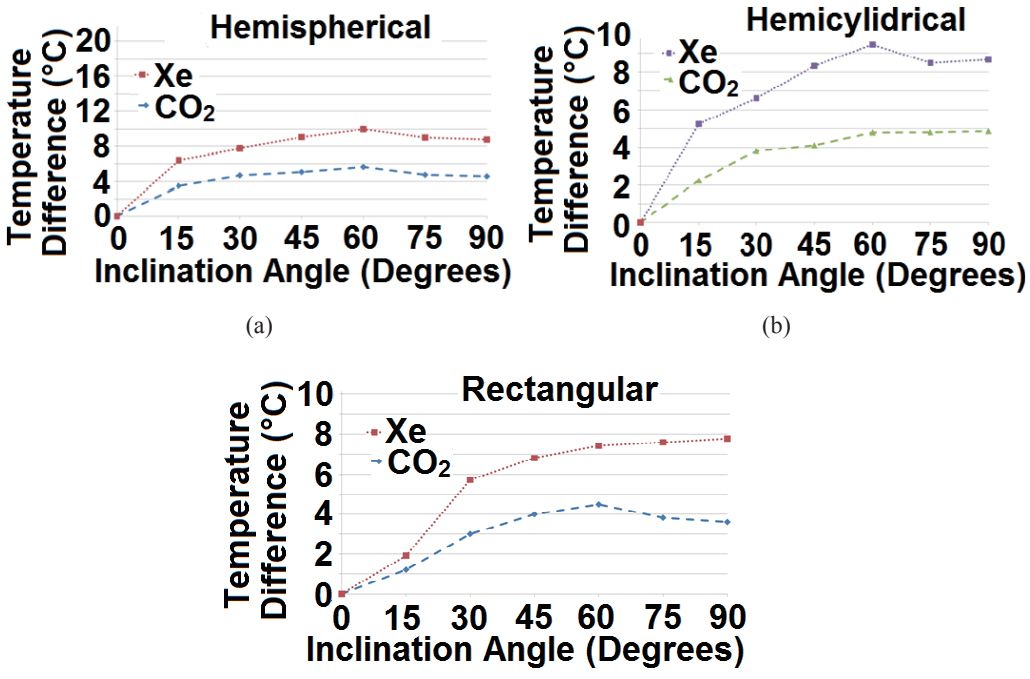

(a) (b)

(c)

Fig. 18. (Color online) Sensitivity curves for nonfloating structures filled with Xe or CO_2 using (a) hemispherical, (b) hemicylindrical, and (c) rectangular chambers.

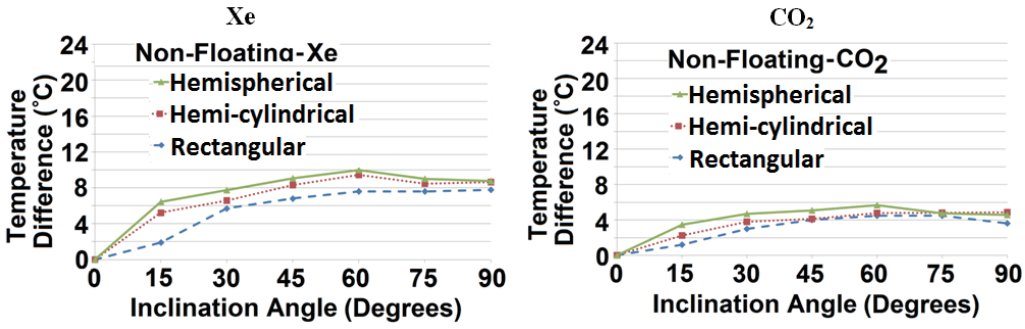

(a) (b)

Fig. 19. (Color online) Sensitivity curves for nonfloating structures filled with (a) Xe or (b) CO_2 gas.

Table 2
Comparisons of sensitivity by filling chamber with Xe or CO_2 gas.

Chamber type	Gas type	A (°C/degree)	Improvement (%)
Rectangular	CO_2	5.196	0.00 (traditional case)
	Xe	8.545	+64.44 (larger)
Hemicylindrical	CO_2	5.543	+6.67 (larger)
	Xe	10.855	+108.89 (larger)
Hemispherical	CO_2	6.697	+28.88 (larger)
	Xe	11.574	+122.74 (larger)

always better than those with a rectangular chamber, because they were more streamlined than the latter. Moreover, if the inclination angles were larger than 60 degrees, then small drops appeared in the sensitivity curves. The theoretical sensitivity curve [temperature (K) vs tilted angle (Θ)] of the inclinometer is a sine wave:

$$K = A\sin(\Theta) \tag{1}$$

Thus A is related to the sensitivity curves in Figs. 19(a) and 19(b), and one can calculate it by using K and Θ in Eq. (1). If Θ is 60 degrees, then the values of A for all combinations of chambers and gases as well as the percentage improvements over the traditional case (with CO_2 and a rectangular chamber) can be obtained and are listed in Table 2. The new sensitivities were improved, and the performance of the case using Xe gas and a hemispherical chamber was the largest, 11.574 °C/deg. That value is better than that of the traditional case with a value of 5.196 °C/deg by 122.74%.

4. Conclusions

Five novel ideas are proposed in this paper for integrating an active RFID tag with thermal convection inertial sensors, such as angular accelerometers, accelerometers, and inclinometers, on a flexible substrate. The first innovative idea was that the inertial sensors would be directly fabricated (or stacked on a layer) on a flexible substrate. The second new idea was that the sensor would be fabricated on a plastic substrate. The third new idea was to use Xe gas in the chamber. The fourth new idea was to further integrate inertial sensors with an active RFID tag on the same substrate.

The final new idea was to apply a hemispherical or a hemicylindrical chamber instead of the conventional rectangular one. The performance (such as reliability, power consumption, wireless ability, and life cycle) of the new device was improved. The results show that the nonfloating inertial sensors may be a good choice not only because of their reliability and cost but also because of their improved performance.

Acknowledgements

We thank the National Science Council for Grant Nos. NSC 101-2622-E-216-001-CC3, 101-2221-E-216-006-MY2, 101-2221-E-216-019, and 102-2622-E-216-002-CC2, and the Ministry of Science and Technology for Grant No. MOST 103-2221-E-216-022. We also thank the National Center for High-Performance Computing (NCHC) for computer time and facilities, including the ESI-CFD+ software package.

References

1 B. Alain, R. Alain, V. Bernard, and G. Alain: European Patent No. 1550874 (2010).
2 G. Piazza and P. Stephanou: Micromechanical Thermo-Fluidic Single-Axis Yaw Rate Sensor (University of California Berkeley, USA, 2002).
3 J. Bahari and A. M. Leung: J. Micromech. Microeng **21** (2011) 1.
4 J. Courteaud, N. Crespy, P. Combette, B. Sorli, and A. Giani: Sens. Actuators, A **147** (2008) 75.
5 J. Dido, P. Loisel, and A. Renault: U. S. Patent No. 7426862 B2 (2008).
6 F. Peluso, D. Castagnolo, and C. Albanese: Microgravity Sci. Technol. **13** (2002) 41.
7 J. M. Lin and C. H. Lin: Proc. 2013 Int. Conf. Comput. Netw. Commun. Eng. (Beijing, 2013) pp. 569–572.
8 Khoshnoud and C. W. de Silva: IEEE Instrum. Meas. Mag. **15** (2012) 14.
9 A. Garraud, A. Giani, P. Combette, B. Charlot, and M. Richard: Sens. Actuators, A **170** (2011) 44.
10 Y. Zhao, A. P. Brokaw, M. E. Rebeschini, A. M. Leung, G. P. Pucci, and A. Dribinsky: U. S. Patent No. 6795752 B1 (2004).
11 Y. Zhao, A. Leung, M. E. Rebeschini, G. P. Pucci, A. Dribinsky, and Y. Cai: U. S. Patent No. 7305881 B2 (2007).
12 A. Dribinsky, G. P. Pucci, Y. Cai, M. O'Brien, G. J. Varghese, Y. Zhao, and Y. Y. Cai: U. S. Patent No. 7862229 (2011).
13 T. R. Hsu: MEMS & Microsystems (McGraw-Hill Companies Inc., Boston, 2002).
14 K. M. Liao, R. Chen, and B. C. S. Chou: Sens. Actuators, A **130–131** (2006) 282.
15 L. Lin, R. T. Howe, and A. P. Pisano: IEEE J. Microelectromech. Syst. **7** (1998) 286.
16 L. C. Spangler and C. J. Kemp: Sens. Actuators, A **54** (1996) 523.
17 A. Petropoulosa, A. Moschosa, S. Athineosa, and G. Kaltsas: Procedia Eng. **25** (2011) 643.
18 R. Dao, D. E. Morgan, H. H. Kries, and D. M. Bachelder: U. S. Patent No. 5581034 (1996).
19 A. A. Rekik, F. Azaïs, N. Dumas, F. Mailly, and P. Nouet: J. Electron. Test. **27** (2011) 41.
20 T. Mineta, S. Kobayashi, Y. Watanabe, S. Kanauchi, I. Nakagawa, E. Suganuma, and M. Esashi: J. Micromech. Microeng. **6** (2001) 431.
21 U. A. Dauderstadt, P. H. S. de Vries, R. Hiratsuka, J. G. Korvink, P. M. Sarro, H. Baltes, and S. Middelhoek: Sens. Actuators, A **55** (1996) 3.
22 U. A. Dauderstadt, P. M. Sarro, and P. J. French: Solid State Sens. Actuators **66** (2008) 244.
23 B. Luo, Z. X. Li, Z. Y. Guo, and Y. J. Yang: J. Micromech. Microeng. **11** (2001) 504.
24 A. H. Ma and A. M. Leung: Proc. IEEE Sens. (2008) p. 1492.
25 G. Daia, M. Li, X. P. He, L. M. Du, B. B. Shao, and W. Su: Sens. Actuators, A **172** (2011) 369.
26 L. A. Rocha, C. S. Silva, M. F. Cerqueira, J. F. Ribeiro, L. M. Goncalves, A. J. Pontes, and J. C. Viana: Procedia Eng. **25** (2011) 607.
27 Y. Hua, Z. Li, and H. Xaio: U. S. Patent No. 8011226 B2 (2011).
28 R. Zhu, H. Ding, Y. Su, and Y. Yang: Sensors **10** (2010) 8304.
29 T. Dau, D. V. Dao, T. Shiozawa, H. Kumagai, and S. Sugiyama: J. Micromech. Microeng. **16** (2006) 1301.
30 A. Ya'akobovitz and S. Krylov: IEEE J. Sens. **10** (2010) 1311.